Unveiling the stability of encapsulated Pt catalysts using nanocrystals and atomic layer deposition

Gennaro Liccardo[1,2], Melissa Cendejas[3], Shyama C. Mandal[1,2], Michael L. Stone[1], Stephen Porter[4], Bang T. Nhan[5], Abinash Kumar[6], Jacob Smith[6,7], Philipp N. Plessow[8], Lynette Cegelski[5], Jorge Osio-Norgaard[1], Frank Abild-Pedersen[2], Miaofang Chi[6], Abhaya K. Datye[4], Stacey F. Bent[1,2]* and Matteo Cargnello[1,2]*

[1]Department of Chemical Engineering and SUNCAT Center for Interface Science and Catalysis, Stanford University, Stanford, CA 94305 (USA)
[2]SLAC National Accelerator Laboratory, Menlo Park, CA 94025 (USA)
[3]Stanford Synchrotron Radiation Lightsource (SSRL), SLAC National Accelerator Laboratory, Menlo Park, CA 94025 (USA)
[4]Department of Chemical and Biological Engineering, University of New Mexico, Albuquerque, NM 87131 (USA)
[5]Department of Chemistry, Stanford University, Stanford, CA 94305 (USA)
[6]Oak Ridge National Laboratory, Oak Ridge, TN 37830 (USA)
[7]Department of Materials Science and Engineering, North Carolina State University, Raleigh, NC 27695 (USA)
[8]Karlsruhe Institute of Technology, Eggenstein-Leopoldshafen, 76344, Germany

*Corresponding authors: sbent@stanford.edu; mcargnello@stanford.edu

ABSTRACT

Platinum exhibits desirable catalytic properties, but it is scarce and expensive. Optimizing its use in key applications like emission control catalysis is important to reduce our reliance on such a rare element. Supported Pt nanoparticles used in emission control systems deactivate over time because of particle growth in sintering processes. In this work, we shed light on the stability against sintering of Pt nanoparticles supported on and encapsulated in Al_2O_3 using a combination of nanocrystal catalysts and atomic layer deposition (ALD) techniques. We find that small amounts of alumina overlayers created by ALD on pre-formed Pt nanoparticles can stabilize supported Pt catalysts, significantly reducing deactivation caused by sintering, as previously observed by others. Combining theoretical and experimental insights, we correlate this behavior to the decreased propensity of oxidized Pt species to undergo Ostwald ripening phenomena because of the physical barrier imposed by the alumina overlayers. Furthermore, we find that highly stable catalysts can present an abundance of under-coordinated Pt sites after restructuring of both Pt particles and alumina overlayers at high temperature (800 °C) in C_3H_6 oxidation conditions. The enhanced stability significantly improves the Pt utilization efficiency after accelerated aging treatments, with encapsulated Pt catalysts reaching reaction rates more than two times greater than a control supported Pt catalyst.

INTRODUCTION

The remarkable catalytic properties of platinum group elements (PGEs) have been known for over a century, with platinum the first metal to be used as a catalyst on an industrial scale for the conversion of SO_2 to SO_3[1]. PGEs have since found numerous applications in many areas, from emission control to pharmaceutical production[2,3]. However, their scarcity and geopolitical distribution make them vulnerable to supply chain disruptions and price fluctuations[2–4]. It is estimated that more than 90% of the world's PGEs reserves are in South Africa, much ahead of the second largest global producer, Russia[5]. Consequently, there is a dire need for research to improve the utilization efficiency of these critical materials and reduce our reliance on these precious metals.

Automotive catalytic converters are responsible for more than half of the global demand for PGEs[6–8]. This demand is mainly driven by the deactivation of the catalyst over time, especially in the first few thousand miles. The deactivation is mitigated by adding more metal than would be necessary to comply with emissions regulatory standards for the required lifetime of the converter[9,10]. Said metals can later be recovered only via chemically harsh and often energy intensive processes[11–13]. The exhaust system exposes the catalyst to a high temperature oxidative environment in the presence of water. In these conditions, supported metal nanoparticles tend to grow larger in size due to sintering driven by the high surface energy of small particles. Sintering can occur because of two phenomena: particle migration and coalescence, and/or Ostwald ripening,[14–16] and results in loss of active surface area and, therefore, a decrease in PGE utilization efficiency. Understanding and preventing this phenomenon clearly represents an important opportunity to reduce the use of scarce and precious PGEs and has been the focus of many researchers.

Particle migration and coalescence, as the name suggests, involves the movement of entire particles across the support's surface, and encompasses their agglomeration into larger ones with decreased surface energy. This phenomenon is typically observed at temperatures above the Tammann temperature of a certain metal, where bulk diffusion can occur[17]. In contrast, Ostwald ripening involves the migration of adatoms or molecular entities between smaller and larger nanoparticles, ultimately yielding larger nanoparticles, like in particle migration and coalescence. Ostwald ripening has been shown to occur at varied temperatures and both through the vapor phase (characteristic of more volatile species) and through the support surface[18,19]. These phenomena can lead to a loss of more than 50% of the original Pt loading, polluting the environment while wasting a precious resource[20,21]. In the first stages of sharp deactivation of supported PGE catalysts via sintering at elevated temperatures, Ostwald ripening has been shown to be the dominant phenomenon[22]. Understanding the causes related to particle migration and coalescence- and Ostwald ripening-induced sintering in catalytic systems and studying methods to avoid them is of great importance in ensuring long-term catalytic stability and optimal PGEs utilization. Many strategies have been employed to limit sintering of PGEs including, but not limited to, exploiting strong metal-support interactions (SMSI)[23–30], compartmentalization of the supported phase[31–33], and encapsulation of nanoparticles within oxide layers[34–40].

In the case of SMSI in emission control catalysts, different works have shown how CeO_2 can be used as a support to induce SMSI with both Pt and Pd, improving the thermal stability of the catalyst while also boosting its activity[19,27,28,41]. However, the benefits of such interactions are limited to the stability of the support, and ceria itself does not withstand thermal aging above 800 °C, as it sinters and loses active surface area [42]. Alternatively, ceria-zirconia as a support has been shown to provide greater thermal resistance while still providing the benefits of CeO_2[43–45]. More recently, alternative supports like boron nitride have also been shown to be able to produce SMSI with supported Pt and Pd nanoparticles, greatly improving the sintering resistance of the catalyst[23,24].

Compartmentalization solutions instead rely on highly engineered supports which allow greater physical separation of the supported nanoparticles. This approach has proven to be very successful as it reduces the likelihood of sintering by increasing diffusion length of monomers between particles. However, it has been mostly explored with non-volatile oxides like PdO[31,32] or, in the case of more volatile ones like PtO_2, it is limited to very low weight loadings[33] (< 0.1 weight %).

Lastly, encapsulation strategies have employed both wet-chemistry routes as well as vapor-phase deposition techniques. In the first case, nanoparticles are embedded in an oxide support either via direct growth of oxide shells around supported nanoparticles[37,38], or using sacrificial polymeric templates that initially host the nanoparticles and are subsequently infiltrated with the oxide precursor[34]. Alternatively, vapor phase deposition techniques like atomic layer deposition[35] (ALD) and molecular layer deposition[39] (MLD), which allow for conformal deposition of thin films, have been used to successfully encapsulate supported nanoparticles (Pd and Pt) within oxide layers that can be grown with these techniques. These different encapsulating approaches share the same outcome of greatly stabilizing the active phase albeit while generally reducing, at least to some extent, the initial activity of the catalyst. Recent work from our group showed that it is possible to achieve highly stable and equally active encapsulated Pt catalysts[34]. Two possible hypotheses have been put forward to explain this behavior. The first one is the stabilization of undercoordinated sites of the supported nanoparticles after encapsulation, like previously reported for Pd nanoparticles[35]. The second one is the added presence of a physical barrier inhibiting the transport of species responsible for sintering (PtO_2 in the case of Pt). However, there is no clear consensus on what drives the very high thermal stability of these systems.

In this work, we shed light on the sintering stability of encapsulated Pt catalysts that were produced via an encapsulation approach that preserves the high activity of supported metal particles[34]. Our strategy consists of creating encapsulated catalysts through fine engineering of the encapsulation environment using a combination of colloidal nanocrystals and ALD techniques. We supported colloidally synthesized Pt nanoparticles on amorphous alumina synthesized via a templated nanocasting method described elsewhere[34] (Pt/Al_2O_3) and followed the evolution of the supported particles before and after hydrothermal aging. ALD is used to controllably encapsulate the supported Pt particles within tunable amounts of an alumina overlayer. By varying the parameters in the Al_2O_3 deposition processes, two distinct levels of encapsulation are obtained, producing thinner or thicker oxide layers around the supported metal particles. In one case, very small amounts of alumina are deposited on the catalyst, obtaining a material with nearly unchanged bulk composition (only adding 3% to the total catalyst mass). In another case, the process yields a more substantial oxide growth, which resulted in a bulk compositional change (adding 10% to the total catalyst mass). The results show that in both cases sintering is significantly reduced, ultimately producing more active catalysts after aging. This work further demonstrates that small amounts of aluminum oxide encapsulating Pt nanoparticles can inhibit the vapor phase transport of PtO_2, which results in the prevention of sintering, ultimately improving catalyst stability and utilization efficiency of Pt for emission control catalysis.

EXPERIMENTAL SECTION

Synthesis of supported catalyst

Alumina was prepared following a previously reported procedure[34]. Briefly, a porous organic framework (POF) was first synthesized[46], and this material was then infiltrated with aluminum nitrate and calcined at 600 °C, removing the POF template while forming the porous alumina.

The POF was prepared using standard air-free Schlenk techniques. 9.3 g of melamine (99%, Acros Organics) and 15 g of terephthalaldehyde (99 %, Acros Organics) were added to 495 mL of dimethyl sulfoxide (99.9%, Fisher) in a 3-neck flask. The content was degassed at room temperature for 15 min, subsequently flushed with nitrogen, heated to 180 °C at a rate of 20 °C min^{-1} and kept at this temperature for 72 hours. The product was then washed with acetone three times and dried under vacuum (~150 torr) at 80 °C for 24 h.

18 g of $Al(NO_3)_3 \cdot 9H_2O$ (>98%, Sigma Aldrich) was dissolved in 100 mL of ethanol. 1.2 g of POF was added to the solution. The mixture was sonicated for 10 min. Ethanol was slowly removed in a rotary evaporator at 60 °C (water bath temperature) at 900 mbar for 1 h and then at 150 mbar for 1 h. The material was dried under vacuum (~150 torr) at 80 °C for 24 h. The final support was obtained by calcining the sample at 600°C for 5 h with a ramp rate of 0.5 °C min^{-1}.

5 nm Pt nanocrystals were synthesized using standard Schlenk line techniques[41] and then impregnated on the alumina support. Pt nanoparticles (NPs) were prepared by thermal decomposition of platinum(II) acetylacetonate ($Pt(acac)_2$, 99.98%). All chemicals were purchased from Sigma Aldrich. 10 mL of trioctylamine (TOA, 95%), 0.66 mL of 1-oleylamine (OLAM, 70%), and 2.5 mL of oleic acid (OLAC, 90 %) were added to 78.8 mg of $Pt(acac)_2$ in a 3-neck flask. The reaction content was degassed (<2 Torr) for 15 min at room temperature. Then 220 μl of trioctylphosphine (TOP, 97 %) were added to the reaction content. The flask was further degassed at 120 °C for 30 min, then it was flushed with nitrogen, heated to 350 °C at a rate of 20 °C min^{-1} and kept at this temperature for 15 min. The content was split into two portions and each portion was washed with 30 mL of isopropyl alcohol and recovered by centrifugation (8000 rpm, 3 min). Finally, the NPs were dispersed in hexanes. An appropriate amount of Pt NPs in hexanes was added dropwise to Al_2O_3 dispersed in hexanes under vigorous stirring. The mixture was stirred for 20 min to allow the NPs to adsorb to the support and the solvents were removed by centrifugation (8000 rpm, 3 min). Colorless supernatant was observed, indicating complete adsorption of the NPs. The powder was dried under vacuum (~150 torr) at 80 °C for 24 h. Colloidal ligands were removed by means of a fast calcination procedure at 700 °C for 30 s in air[47].

Synthesis of ALD-modified catalysts

ALD was performed in a commercial reactor (Arradiance Gemstar 6) using trimethylaluminum ($AlMe_3$ - Sigma-Aldrich) and de-ionized water as precursors for alumina deposition. 50 ALD cycles were performed on the starting catalyst in both the *Short Exposure* and *Long Exposure* samples. The two ALD recipes differ in precursors pulse length and deposition chamber temperature, as summarized in Table 1. A thin bed of catalyst powder (150 mg) was laid onto a stainless-steel holder[48], which was then cleaned via a UV-ozone treatment (PSD Series – Digital UV Ozone System by Novascan, wavelengths 185 nm and 254 nm) for 15 minutes. Before every run, the holder was kept in the vacuum chamber for 1 h to purge the reactor and allow the powder to reach the deposition temperature. N_2 was used as a carrier gas. N_2 flow was kept at 10 mL min^{-1} throughout the run except when it was increased to 60 mL min^{-1} for purging steps. A soak step indicates time spent without pumping the ALD chamber, allowing for precursor diffusion through the powder. The reactor was pumped by a Leybold Trivac S8B/WS (102 55A) pump and its base pressure ranged between 150 and 200 mTorr.

Table 1. ALD process conditions for the two distinct methods used in this study.

Step	Short Exposure method	Long Exposure method

Temperature	125 °C	200 °C
$AlMe_3$ pulse	30 ms	400 ms
Soak	100 s	
Purge	180 s	
Water pulse	30 ms	4000 ms
Soak	100 s	
Purge	180 s	

Catalytic testing

The catalysts were tested in a U-shaped quartz plug flow reactor with 1 cm diameter at ambient pressure. Catalyst powder (20 mg) was mixed with SiC diluent (acid washed, sieved < 180 µm, 180 mg) and loaded into the reactor between two layers of acid-washed, calcined quartz (180-450 µm sieved). The catalyst bed was packed to a length of 1 cm. The reactor was heated in a Micromeritics Eurotherm 2416 furnace with a K-type J-Kem thermocouple probe placed in the center of the bed. Gas reactant mixtures were prepared by mixing C_3H_6 (5 vol. % in Ar, Airgas Certified), O_2 (5 vol. % in Ar, Certified Airgas) and Ar (99.999% Airgas) through mass flow controllers (Brooks SLA5850). The mixtures flowed through a heated (30 °C), de-ionized water bubbler to introduce steam. Before each catalytic measurement, diluted catalyst beds were placed under a flow of 5 vol. % O_2 in Ar at a rate of 50 mL min^{-1} at 300 °C for 30 min. Aging of the catalysts was performed *in situ*, ramping at 10 °C min^{-1} to 800 °C, holding at that temperature for 2 hours, and cooling to 120 °C at 10 °C min^{-1} in a mixture of 0.15 vol. % C_3H_6, 3 vol. % O_2, 4.2 vol. % H_2O in Ar. Gas reactants and products for rate measurements were analyzed using an online gas chromatograph (GC, Buck Scientific model 910) equipped with a methanizer and a flame ionization detector. The gas hourly space velocity (GHSV) was varied to achieve C_3H_6 conversion for each measured rate that was less than 10%. Each data point was taken at steady state (representative experimental raw data shown in Figure S1) and was the average of at least four GC injections. The reported values are normalized by Pt mass as measured by inductively coupled plasma optical emission spectroscopy (ICP-OES).

Pt volatility measurements

To accurately quantify the volatility of the Pt species, a thin film of each catalyst was deposited onto Si wafers. The film was created by grinding 50 mg of the catalyst, mixing it with 2 mL of ethanol, and depositing it onto silicon wafers using a pipette. The dispersion was then spin-coated at approximately 2500 rpm to form a thin film. To simulate real-world aging conditions for diesel oxidation catalysts (DOCs), wafers were loaded into quartz tubes in a furnace at 800 °C. Aging involved flowing air at 50 $mL \cdot min^{-1}$ and rapid cooling upon opening the furnace. The aging times reported reflect only the duration at the aging temperature. Post-aging, XRF analysis was used to quantify metal loading.

Structural characterization

High-angle annular dark-field (HAADF) scanning transmission electron microscope (STEM) imaging was performed with a probe-corrected JEOL NEOARM operated at 200 KV with a probe convergence semi-angle of 28 mrad. Pt particle size distributions were obtained by manually measuring at least 150 nanoparticles in HAADF-STEM images using image analysis software ImageJ.

Inductively coupled plasma optical emission spectroscopy (ICP-OES) measurements were performed by Galbraith Laboratories Inc. as follows: 25 mg of sample material was prepared by hot block digestion in 25 mL of 3:3:1 HNO_3:HCl:HF until fully dissolved. Following digestion, a portion of the solution was further diluted by 10 times and used for analysis of Al. Pt was analyzed in the undiluted solution. Analysis by ICP-OES was then conducted on a PerkinElmer Avio 500 ICP Optical Emission Spectrometer. The spectral lines used for quantitation of Pt and Al were 265.945 nm and 396.153 nm, respectively. Scandium was used as internal standard and analyzed at 361.383 nm. Each instrumental reading was conducted in triplicate and averaged.

X-ray fluorescence (XRF) measurements were carried out using an Orbis Micro-XRF Analyzer operated in a vacuum with a Rh source and a 30 mm^2 Silicon Drift Detector. XRF analysis utilized settings of 25 kV and a current range of 800-900 μA such that the dead time was kept between 30-50%. A consistent 30 μm spot size probe and a working distance of approximately 77 mm were maintained for a uniform analysis area across measurements. Three standards were employed to ensure accurate quantification. Each sample underwent analysis across five different areas, with mean composition reported as a weight percentage referenced to the alumina support. Consistent with recommendations by Schweitzer *et al.*[42], for experimental rigor and reproducibility, three standards were employed with each measurement to ensure accurate quantification. The variability in the XRF results is represented by the error bars due to the nonuniform sample thickness on the Si wafer.

X-ray fluorescence (XRF) measurements reported in the SI were carried out using a Spectro Xepos HE XRF Spectrometer. The samples were measured together with a set of 5 standards obtained by physically mixing alumina and platinum(II) acetylacetonate ($Pt(acac)_2$, 99.98%), with Pt weight % ranging from 0 to 1.5 % nominally. The same mass of catalyst was loaded in the sample holder for each sample (250 mg).

X-ray photoelectron spectroscopy (XPS) measurements were performed using a PHI VersaProbe 3 with an Al kα source. Powder samples were carefully fixed to a 2 inches platen by double sided tape. An ion gun and an electron neutralizer gun were used to compensate for charging during the measurement. Spectra were obtained with pass energy of 55 eV and a step of 0.05 eV.

X-ray diffraction (XRD) measurements were performed using a Rigaku MiniFlex600 with a Cu source (wavelength 1.54059 Å). Powder samples were dispersed in ethanol before being drop casted onto sample holders and dried prior to measurement. Measurements used a start angle of 3° and an end angle of 90° with a step of 0.01° and a dwell time of 0.75 seconds. The operating voltage was 40 kV while the current was 15 mA.

In situ Pt L3 X-ray absorption spectroscopy (XAS) was conducted at beamline 2-2 at the Stanford Synchrotron Radiation Lightsource (SSRL). Beamline 2-2 is the center branch of a bent magnet source with a water-cooled double crystal monochromator equipped with a Si(220) crystal set (crystal orientation $\varphi = 90°$). Data were collected in step scan mode (ca. 15 min per scan) using fluorescence geometry with a PIPS diode and nitrogen filled ion chambers. A Pt foil was scanned simultaneously for energy calibration. For each experiment ca. 30 mg of catalyst (125-180 μm mesh) was packed into a 3 mm outer diameter quartz capillary to yield a 10 mm long catalyst bed with quartz wool on either side. A K-type thermocouple was placed touching the end of the catalyst bed and gas flow rates were set using calibrated mass flow controllers. Gas flows and temperature were controlled through a LabView interface. The reactor effluent was monitored by an online mass spectrometer.

N_2 physical adsorption measurements were performed using a Micromeritics 3Flex. Brunauer-Emmett-Teller (BET) theory was used to determine specific surface area, and Barrett-Joyner-Halenda (BJH) theory was use for pore size distribution analysis. 100 mg of catalyst were loaded in a quartz tube. Prior to the measurement, the samples were degassed in vacuum at 150 °C for 19 h to remove any adsorbates from the catalyst's surface. The temperature was kept relatively low to avoid major restructuring of the ALD films. For every sample an adsorption and desorption isotherm were collected at liquid N_2 temperature (-195.8 °C).

In-situ diffuse reflectance infrared Fourier-transform spectra (DRIFTS) were recorded using a Thermo Fisher Scientific Nicolet iS50 spectrometer with a liquid-nitrogen-cooled MCT detector, a Harrick Praying Mantis DRIFTS accessory, and a high-temperature experimental cell. A single spectrum consisted of 32 scans with 4 cm^{-1} resolution and took 18 s to collect. Gas flow rates were controlled using calibrated mass flow controllers, and gases were analyzed by a mass spectrometer at the cell outlet. Each sample was pretreated at 300 °C for 30 minutes under 20 % O_2 by volume in He followed by 30 minutes under 10 % H_2 by volume in He before cooling to room temperature (18 °C) to perform CO adsorption measurements. In each experiment, 10 % CO by volume in He was added to the cell (20 $mL \cdot min^{-1}$) until there was no change in the intensity of the gas-phase signal (~5 min). The cell was then flushed with He (20 $mL \cdot min^{-1}$) to remove the gas-phase CO before spectral collection. CO DRIFTS were collected in difference mode, with the room temperature spectrum of the pretreated sample serving as the background.

Solid state nuclear magnetic resonance (SSNMR) spectroscopy measurements were performed using an 89-mm bore 11.7 T magnet and custom-built 4-frequency all-transmission-line NMR probe with active control of radiofrequency amplitudes and a 2kW pulsed amplifier (American Microwave Technology Model 3445), controlled by a Varian VNMRS console with VNMRJ software. Samples were spun at 7143 ± 3 Hz at room temperature in thin walled 5 mm outer diameter zirconia rotors. Direct polarization experiments were performed for ^{27}Al (with Larmor frequency 130 MHz) using a 3 ms $\pi/2$ pulse and a recycle delay of 1 s. Results were similar with smaller (15-20 degree) tip angle. Each spectrum was the result of 4096 or 8192 scans. ^{27}Al chemical shift was referenced to external $Al_2(SO_4)_3$. Free induction decays were processed using 80 Hz exponential line broadening prior to Fourier transformation.

Theoretical calculations

The surfaces of 4-layer 3×3 Pt(111) and 8-layer 3×3 Pt(211) (Figure S2) were analyzed to investigate the distinctive properties of both terrace and step sites on Pt nanoparticles. The surfaces were subjected to first principles density functional theory (DFT) calculations, employing the Vienna Ab initio Simulation Package (VASP 5.4.4) within the Atomic Simulation Environment (ASE)[49–52]. The BEEF-vdW functional, known for its accurate adsorbate binding energy calculations on transition metal surfaces, was utilized to account for exchange-correlation effects[53–55]. The plane wave basis sets were constrained with a cutoff energy of 500 eV, and structural optimizations were conducted until total energies converged to a minimum of 10^{-5} eV and forces reached levels below 0.05 eV/Å. For the Pt(111) surface, the bottom two layers were held fixed while the upper layers underwent relaxation during system optimization. In the case of the Pt(211) surface, the bottom four layers were fixed, and relaxation of the upper layers was carried out during optimization. To prevent periodic image interactions, a vacant space of more than 15 Å was introduced between the slabs. The Monkhorst−Pack method was employed to generate k-point grids in Brillouin zone[56]. Solving the DFT-based Kohn-Sham equations entailed using a 4×4×1 k-point grid to account for reciprocal space on the surfaces. To counteract artificial periodic interactions between slabs[57], a dipole correction was applied. The lattice parameter was optimized, yielding a Pt lattice constant value of 3.98 Å, consistent with prior investigations[58,59]. In the analysis of gas phase molecules, a cell measuring 21×22×23 Å was employed, and optimizations were performed for energy calculations, using a 1×1×1 k-point density. Additionally, the binding energies of metal atoms were determined utilizing the equation (i):

$$\Delta E_A = E_{slab+A} - (E_{slab} + E_A) \qquad \text{(i)}$$

Where ΔE_A is the binding energy of adsorbates, E_{slab+A}, E_{slab}, and E_A represent the optimized total energy of the slab with adsorbates, optimized total energy of the slab, and optimized total energy of the adsorbates, respectively. Reaction free energies were determined by factoring in the correction for zero-point vibrational energy and entropy at the specified temperature, as described by the equation (ii):

$$\Delta G = \Delta H - T\Delta S \qquad \text{(ii)}$$

In the above equation (ii), ΔG, ΔH, and ΔS are the reaction free energy, change in total enthalpy, and change in entropy of the considered elementary step, respectively, at temperature T. Entropy calculations were conducted using equation (iii):

$$S = N_A k_B \sum \left(\frac{\frac{hn_i}{k_B T}}{\exp\left[\frac{hn_i}{k_B T}\right] - 1} - \ln\left[1 - \exp\left[-\frac{hn_i}{k_B T}\right]\right] \right) \qquad \text{(iii)}$$

Where S is the entropy, N_A is the Avogadro's constant, and k_B is the Boltzmann's constant. The chemical potential of O_2 was computed employing equation (iv)[60]:

$$\mu_{O_2} = E^{O_2,gas} + E_{ZPE}^{O_2,gas} - TS_{O_2,gas} + k_B T * \ln\left[\frac{p_{O_2,gas}}{100000\ Pa}\right] \qquad \text{(iv)}$$

μ_{O_2} is the chemical potential of O_2, $E^{O_2,gas}$ is the O_2 gas phase energy, $E_{ZPE}^{O_2,gas}$ is the zero-point vibrational energy of gas phase O_2, $S_{O_2,gas}$ is the O_2 gas phase entropy. Along with this, we considered various oxygen coverages and created a differential phase diagram following equation (v)[52].

$$\Omega_{diff} = E^{slab+N\cdot O^*} - E^{slab+(N-1)\cdot O^*} + E_{ZPE}^{slab+1O^*} - T \cdot S_{1O^*} - \frac{1}{2}\mu_{O_2} \qquad \text{(v)}$$

Ω_{diff} is the potential for various oxygen coverages and temperature. All the optimized structures and binding energies of adsorbates can be found in cathub[61].

RESULTS AND DISCUSSION

Catalyst synthesis and characterization

The supported catalysts were prepared starting from an alumina support and colloidally synthesized Pt nanocrystals. Subsequently, the catalysts were encapsulated in alumina overlayers via atomic layer deposition (ALD), where tuning the precursor exposure in the deposition chamber allowed us to control the amount of alumina deposited on the sample. Two conditions were used during the ALD process, labeled Short Exposure (SE) and Long Exposure (LE), which indicated the length of the precursor pulse which ultimately affected the amount of ALD alumina deposition onto the Pt/Al_2O_3 catalyst. Short Exposure and Long Exposure samples are abbreviated as SE- Pt/Al_2O_3 and LE- Pt/Al_2O_3, respectively. The two different types of encapsulated samples were characterized and tested for hydrothermal stability in a relevant reaction environment. The catalysts before and after the hydrothermal treatment were labeled as "fresh" (F) and "aged" (A), respectively. As an example, the sample A-LE-Pt/Al_2O_3 refers to the Pt/Al_2O_3 modified by Long Exposure ALD and after hydrothermal aging. These modified catalysts were benchmarked against the Pt/Al_2O_3 sample that was not modified by ALD.

To probe for structural changes of the Pt nanoparticles before and after ALD, HAADF-STEM imaging was performed. Size distributions of the Pt nanoparticles were obtained (Figure 1). F-Pt/Al_2O_3 showed an average particle size of 4.7±0.8 nm. F-SE-Pt/Al_2O_3 sample displayed an average particle size of 4.8±0.5 nm while for F-LE-Pt/Al_2O_3, the size was 4.8±0.8 nm. These observations revealed that the Pt particle size distribution remained unchanged after the ALD process was performed on the starting catalyst, preserving the initial nature of the Pt nanoparticles. Because the alumina deposition by ALD was performed on particles that were already supported onto alumina, it was not possible to obtain any contrast difference to clearly distinguish the added encapsulating layer via HAADF-STEM imaging.

The bulk and surface compositions of the catalysts were determined to measure the amount of alumina grown by ALD. Specifically, ICP-OES and XRF were used to obtain the bulk composition of the catalysts. Al/Pt mass ratios were calculated since alumina was deposited by ALD. The F-Pt/Al_2O_3 sample showed an Al/Pt mass ratio of 92.2±0.7, the F-SE-Pt/Al_2O_3 sample showed a ratio of 95.4±1.0, while the F-LE-Pt/Al_2O_3 sample showed a ratio of 101.2±1.0 (Table 2). These changes corresponded to a mass increase of 3.3% for F-SE-Pt/Al_2O_3 and 9.7% for F-LE-Pt/Al_2O_3 after ALD. These measurements highlighted how a smaller amount of alumina was deposited via the *Short Exposure* method, while a significant amount was grown via the *Long Exposure* one. Similar results were obtained from XRF measurements (Table S1).

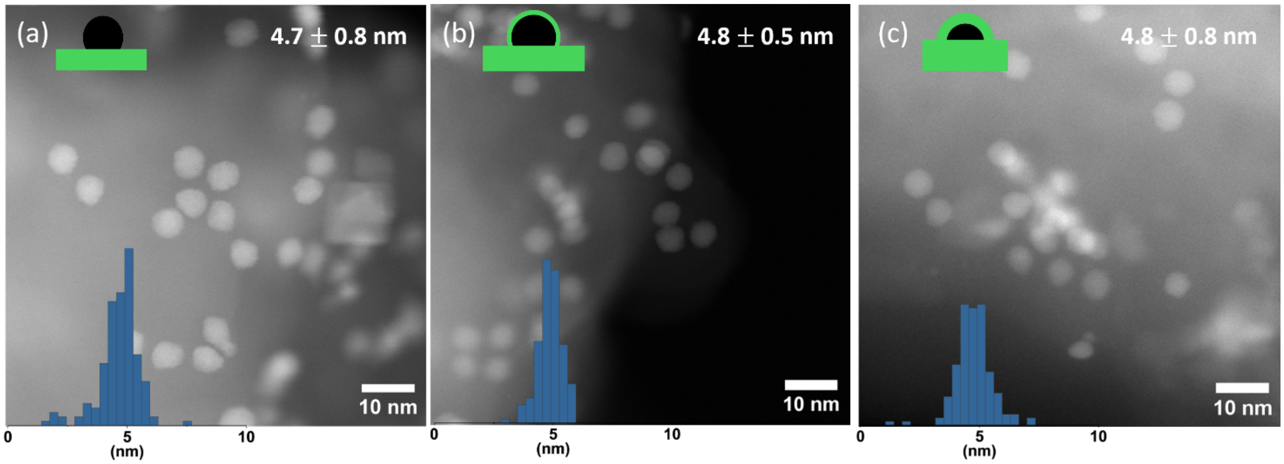

Figure 1. Representative HAADF-STEM images and particle size distributions (histograms in inset) before aging for (a) F-Pt/Al_2O_3, (b) F-SE-Pt/Al_2O_3, and (c) F-LE-Pt/Al_2O_3. Average particle sizes and standard deviations are reported in the top right corner.

Table 2. Al/Pt mass ratio measured by ICP-OES and corresponding mass increase compared to the starting catalyst for Pt/Al_2O_3, SE-Pt/Al_2O_3 and LE-Pt/Al_2O_3.

Sample	**Al/Pt mass ratio**	**Mass increase**
Pt/Al_2O_3	92.2 ± 0.7	N/A
SE-Pt/Al_2O_3	95.4 ± 1.0	3.3 %
LE-Pt/Al_2O_3	101.2 ± 1.0	9.7 %

To investigate surface compositional changes after ALD, XPS spectra of the fresh catalysts were collected. Survey scans detect the presence of Al, O, C for all samples, while Pt is not easily identified even for Pt/Al_2O_3 due to the low weight loading of the catalyst (Figure S3) The most intense Pt signal (Pt 4f) partially overlapped with the Al 2p signal but could still be readily discerned in the F-Pt/Al_2O_3 sample at 70.8 eV (Figure 2). The position of this peak relative to that of Al 2p (found at 74 eV) is indicative of a metallic Pt state[62,63]. This Pt 4f signal was absent in the spectra of both F-SE-Pt/Al_2O_3 and F-LE-Pt/Al_2O_3 recorded across multiple regions of the sample. Because the Pt loading did not drastically decrease after ALD deposition according to the ICP-OES data, we conclude that the Pt XPS signal was absent on the F-SE-Pt/Al_2O_3 and F-LE-Pt/Al_2O_3 samples due to the presence of the ALD alumina overlayers, given that XPS is sensitive to the topmost surface layers. The results suggest the successful deposition of alumina on the Pt surface and encapsulation of Pt nanoparticles in both ALD samples.

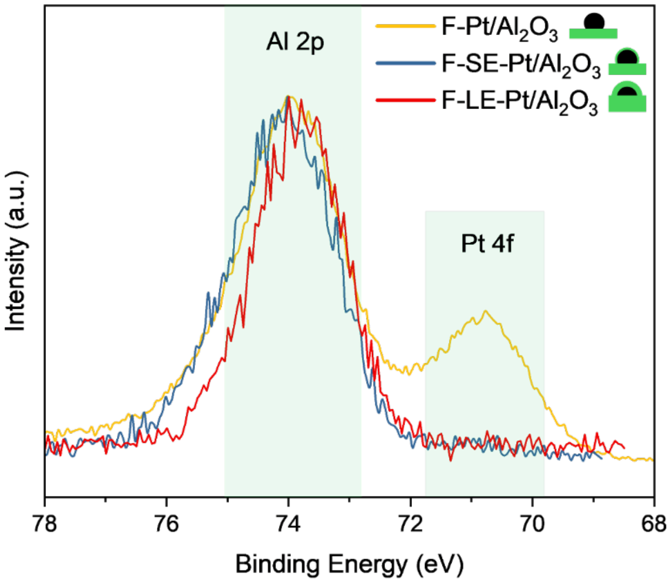

Figure 2. X-ray photoelectron spectra of the Al 2p and Pt 4f regions of F-Pt/Al_2O_3, F-SE-Pt/Al_2O_3 and F-LE-Pt/Al_2O_3.

Ab initio DFT calculations of representative surfaces were used to elucidate the interactions between Pt and alumina during the ALD deposition process. The Pt(111) surface (more coordinated) was used as a model for terrace sites in nanoparticles, whereas the Pt(211) surface (less coordinated) was used as a descriptor for step sites (Figure S1). The binding energies for possible intermediates in the ALD process were calculated (see details in Table S2). The results showed that most of the considered intermediates bind more strongly to step sites than on terrace sites suggesting that the undercoordinated Pt sites had stronger interactions with the alumina ALD intermediates/products, thus likely being more reactive during the ALD process.

All the prepared catalysts were tested for propene complete oxidation as a model reaction in emission control catalysts. Activity was measured before and after a high temperature steam-rich oxidative aging process to test the stability of the catalysts. The aging protocol involved ramping the temperature up to 800 °C for 2 h in excess oxygen and steam. Such conditions are known to favor Pt sintering[9,14,16,22,34]. Rates of propene oxidation (here reported as CO_2 production rate) demonstrated a decreasing trend in activity for the fresh catalysts as follows: F-Pt/Al_2O_3 > F-SE-Pt/Al_2O_3 >> F-LE-Pt/Al_2O_3 (Figure 3). Given that the samples were prepared using the same batch of Pt nanocrystals as precursors, it is unlikely that major differences in the Pt structure occurred during the preparation of the samples, and the HAADF-STEM images confirmed that that particle size distributions were the same across those three samples. This trend instead correlated with the amount of alumina that was deposited during the ALD process, suggesting that some Pt sites were covered with alumina and thus unavailable for reactivity, and that the rate decrease was proportional to the amount of alumina deposited by ALD.

Following the aging treatment, rates for the Pt/Al_2O_3 sample sharply decreased by ~3 times, while the SE-Pt/Al_2O_3 sample retained its activity almost entirely, and the LE-Pt/Al_2O_3 sample greatly activated, with rates that increased by ~10 times. Overall, both ALD samples showed rates after aging that were ~2.5 times higher compared to the aged Pt/Al_2O_3 sample. The rate trend after aging was therefore reversed compared to the activity of the fresh catalysts, with the order A-LE-Pt/Al_2O_3 ≥ A-SE-Pt/Al_2O_3 >> A-Pt/Al_2O_3.

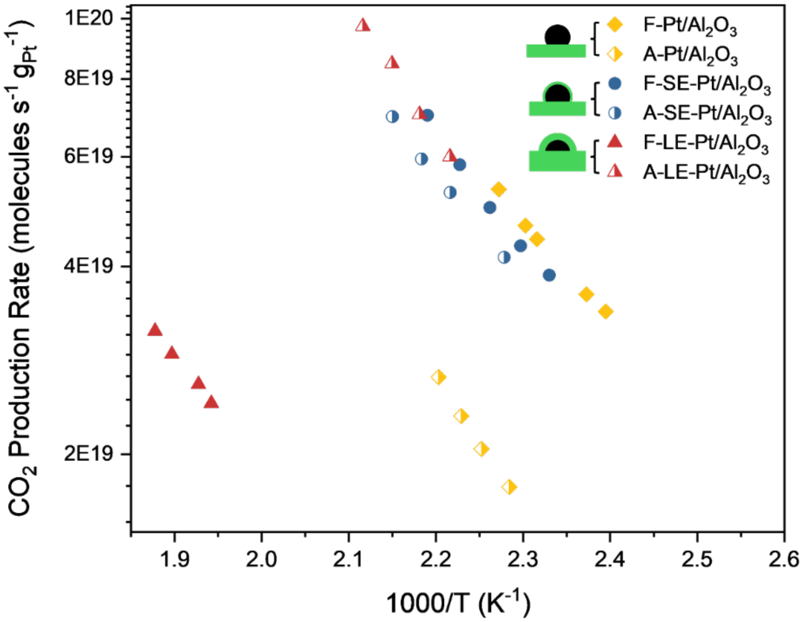

Figure 3. CO_2 production rates normalized by Pt mass as measured by ICP-OES for fresh and aged samples. Reaction mixture: 0.15 vol. % C_3H_6, 3 vol. % O_2, 4.2 vol. % H_2O in Ar. Aged samples were treated under reaction conditions for 2 h at 800 °C prior to testing.

Study of catalyst aging

Sintering is known to be responsible for deactivating supported Pt nanoparticles under oxidative atmosphere at high temperature. HAADF-STEM was used to discern changes in the particle size distribution (PSD) of the aged catalysts (Figure 4). The Pt/Al_2O_3 catalyst showed an increase in average particle size from 4.7 nm to more than 20 nm and a very broad particle size distribution after aging, clearly highlighting that sintering occurred in this sample. On the contrary, both ALD samples showed a nearly preserved particle size after the same aging procedure with average sizes of 4.9 ± 1.6 and 4.3 ± 2.2 nm for SE and LE ALD, respectively, albeit also with a slightly larger particle size distribution compared to the fresh samples. Therefore, sintering was significantly reduced by applying alumina through ALD processes. These results confirmed that even small amounts of alumina added by ALD could greatly prevent Pt sintering under high temperature oxidative conditions. Furthermore, we considered whether the alumina layer prepared via ALD was contributing to the stability of the catalysts. To investigate this aspect, ALD alumina was deposited on the starting support followed by the colloidally synthesized Pt nanoparticles . The results indicated that such a catalyst (labeled Pt/ALD/Al_2O_3) was not stable in our aging conditions, deactivating significantly (Figure S4), with sintered Pt (Figure S5) . This result highlighted that the formation of encapsulating layers via ALD of alumina was the reason for the observed stability.

The average particle size of the LE-Pt/Al_2O_3 catalyst decreased after the aging treatment (from 4.8 nm to 4.3 nm), and smaller than average particles were observed in this sample by HAADF-STEM (Figure S6-7). This observation is evidence of changes occurring to the Pt nanoparticles after aging. Since the alumina ALD deposition was performed at 200 °C, it can be reasonably assumed that substantial changes occurred at the higher temperatures of the aging, as previously observed in other catalysts containing ALD overlayers.[35,39,64] The restructuring of the alumina ALD overlayers in turn affected the encapsulated Pt particles (see below for further discussion). This restructuring led to the formation of smaller Pt particles, which allowed more Pt to be available for the reaction.

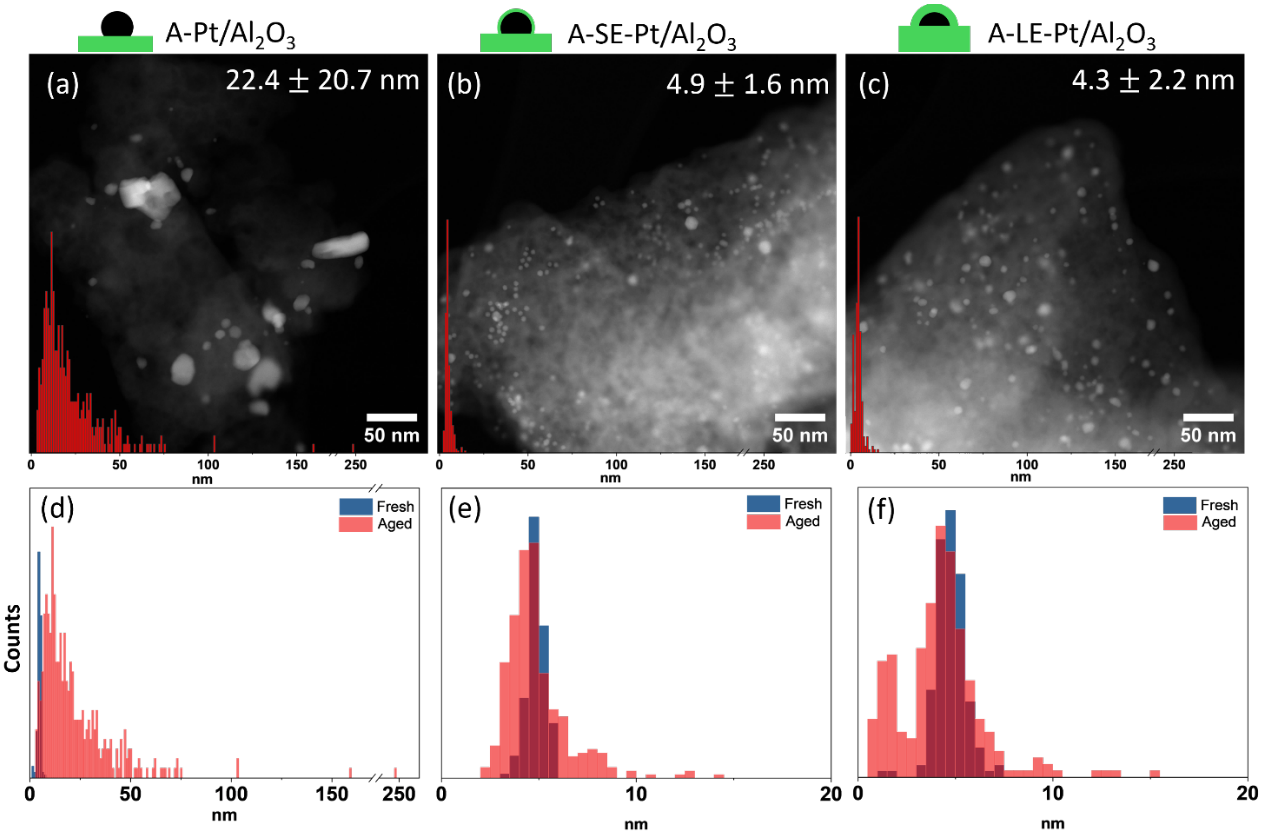

Figure 4. (a-c) Representative HAADF-STEM images of the aged samples: (a) A-Pt/Al_2O_3, (b) A-SE-Pt/Al_2O_3, and (c) A-LE-Pt/Al_2O_3 and overlayed corresponding particle size distribution analysis. (d-f) Particle size distribution analysis comparison for fresh and aged catalysts: (d) Pt/Al_2O_3, (e) SE-Pt/Al_2O_3, and (f) LE-Pt/Al_2O_3. A horizontal axis break in panels a-d was placed between 170-240 nm. Please note the different x-axis range in panels (e) and (f) for clarity. The darker red color in panels d-f indicates overlap of the two particle size distributions.

Nitrogen adsorption studies were performed to analyze surface area and pore size changes of the catalysts due to ALD treatments and aging under reaction conditions (Table 2, Figure S8). The Pt/Al_2O_3 sample specific surface area decreased from 30 to 21 $m^2\ g^{-1}$ after aging. The changes measured for this sample could be attributed to a restructuring of the underlying support, which was initially calcined to 600 °C, after aging at higher temperature. While Pt sintering can lead to a decrease in surface area, its small quantity relative to Al_2O_3 would not justify such a change. In the case of the ALD-modified samples, the introduction of alumina and consequent blockage of pores resulted in an overall lower specific surface area of 17 and 5 $m^2\ g^{-1}$ for the F-SE-Pt/Al_2O_3 and F-LE-Pt/Al_2O_3 samples, respectively. After aging, an increase in specific surface area was observed for both samples to 23 m^2 g^{-1} for A-SE-Pt/Al_2O_3 and to 139 m^2 g^{-1} for A-LE-Pt/Al_2O_3. This result further suggests that there was thermal restructuring of the ALD alumina overlayers leading to a larger specific surface area, as evidenced by a clear change in the pore size distribution (Figure S8). Notably, the A-Pt/Al_2O_3 and A-SE-Pt/Al_2O_3 samples were characterized by a very similar specific surface area, once again pointing at the small changes introduced by the alumina ALD overlayers for this short exposure ALD sample. It is also worth pointing out that any contribution to these results coming from the Pt nanoparticles' surface area can be neglected, as one can expect the metallic area of a 0.5 wt.% catalyst with average particle size of 5nm to be ~0.1 m^2 g^{-1}.

Table 2. Brunauer-Emmet-Teller (BET) specific surface area from N_2 physisorption measurements of the catalysts before and after aging.

Sample	**Specific surface area (m^2 g^{-1}) - Fresh**	**Specific surface area (m^2 g^{-1}) - Aged**
Pt/Al_2O_3	30	21
Short Exposure ALD/Pt/Al_2O_3	17	23
Long Exposure ALD/Pt/Al_2O_3	5	139

^{27}Al solid-state NMR (SSNMR) spectroscopy was performed to characterize the aluminum speciation in the samples before and after aging. 4-, 5-, and 6-coordinated ^{27}Al species were identified at δ_{iso} = 68, 35, and 5 ppm, respectively[65] (Figure 5). The presence of 5-coordinate ^{27}Al indicates that the alumina in the fresh samples is amorphous.[66] The relative intensity of the 5-coordinated ^{27}Al signal (δ_{iso} = 35 ppm) compared to the 6-coordinated ^{27}Al signal (δ_{iso} = 5 ppm) increased in the F-SE-Pt/Al_2O_3 sample compared to the F-Pt/Al_2O_3 sample, and further increased in the F-LE-Pt/Al_2O_3 sample, confirming that the added ALD layers were amorphous. The greater intensity of the 5-coordinate ^{27}Al of F-LE-Pt/Al_2O_3 compared to F-SE-Pt/Al_2O_3 confirms that more amorphous alumina was deposited in the LE ALD process. For all samples, aging resulted in the decrease of signal intensity for the 5-coordinated ^{27}Al, indicating the crystallization of the alumina following aging of the samples.

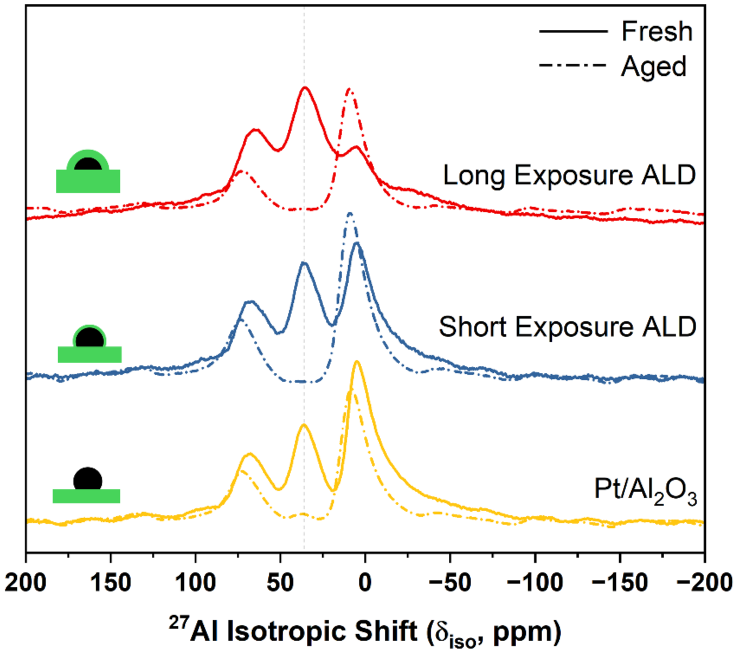

Figure 5. Single pulse ^{27}Al SSNMR spectra of fresh (solid line) and aged (dashed line) catalysts.

XRD patterns of the aged catalysts were collected to identify crystalline phases (Figure S9). A-Pt/Al$_2$O$_3$ showed a clear peak at 81.4° that could be attributed to Pt. The same peak was broader for the ALD-modified samples, consistent with the fact that sintering was inhibited in both cases and the small particles are not expected to yield detectible XRD peaks. Another peak at 85° was observed for the A-LE-Pt/Al$_2$O$_3$ sample. This peak could be ascribed to the formation of crystalline γ-Al$_2$O$_3$, consistent with SSNMR results. Interestingly, this peak was not found in A-Pt/Al$_2$O$_3$, indicating that the ALD alumina was mostly responsible for the formation of this phase. In the pattern for the A-SE-Pt/Al$_2$O$_3$ sample, this peak was not discernible. This observation suggests that an insufficient amount of ALD alumina was deposited to form a crystalline structure like in the case of the A-LE-Pt/Al$_2$O$_3$ sample.

XPS was performed on the aged samples to investigate potential changes in the ALD overlayers (Figure S10). The XPS spectrum of the A-Pt/Al$_2$O$_3$ sample clearly displays a shoulder in the Al 2p peak that can be attributed to Pt 4f, as also seen in F-Pt/Al$_2$O$_3$. In the case of the A-SE-Pt/Al$_2$O$_3$ sample, a weak but detectable Pt 4f peak emerged from the baseline compared to the fresh case (Figure 2), indicating that some Pt could have surfaced after the aging treatment. The A-LE-Pt/Al$_2$O$_3$ sample, instead, showed no major changes compared to the fresh sample, and still no Pt contribution could be found. It is likely that the thicker alumina overlayers in this latter sample made it more challenging for any Pt to migrate to the surface, leading to no Pt signal being detected. These results further confirm the different nature/amount of the alumina deposited by the short and long exposure ALD processes.

In situ XAS measurements were performed on model catalysts to follow potential changes in Pt oxidation state under reaction conditions. The experiments revealed no differences between a supported and an ALD encapsulated Pt catalyst, which both remained metallic throughout the measurement, as the catalysts were heated up to 700 °C (upper temperature limit of the beamline hardware setup) in propene oxidation conditions (Figure S11). These results indicated that the bulk Pt oxidation state was not an important factor in the observed sintering resistance of the encapsulated Pt catalysts.

The Pt speciation was characterized by DRIFTS using CO as a probe molecule (Figure 6). The raw spectra were plotted to illustrate changes to the Pt speciation because of catalyst aging (Figure 6 a-c). The spectra were also normalized in intensity to compare the effect of ALD treatments on the different samples (Figure 6d).

Each fresh sample showed a relatively narrow single feature for CO adsorption that was centered at ~2081 cm^{-1} (total full width at half maximum (fwhm) ~19 cm^{-1}) for F-Pt/Al_2O_3, ~2075 cm^{-1} (total fwhm ~26 cm^{-1}) for F-SE-Pt/Al_2O_3, and ~2073 cm^{-1} (total fwhm ~28 cm^{-1}) for F-LE-Pt/Al_2O_3, indicative of CO linearly bound to metallic Pt sites[67]. The peak center shifted to lower wavenumbers (red shift) and broadened as an effect of increasing ALD coverage. Additionally, the raw spectral intensity decreased with increasing ALD coverage.

After aging, all spectra changed drastically in shape and number of features. In general, all samples presented a sharp, intense peak at high wavenumbers (~2093 – 2087 cm^{-1}, total fwhm ~12-20 cm^{-1}) and broader feature/s at lower wavenumbers (~2070 – 2000 cm^{-1}, total fwhm ~50-100 cm^{-1}). The relative intensity of these two main peaks was sample-dependent, with the intensity of the broad, low-wavenumber feature increasing with ALD coverage.

Looking more deeply at the CO features in the DRIFTS data gave further insights into the surface Pt sites.[6869,70] The peak position of adsorbed CO is sensitive to the Pt coordination environment, and the breadth of the peak is indicative of binding site uniformity, with non-uniform binding sites resulting in broader peaks[71]. For metallic Pt^0, the vibrational frequency of adsorbed CO decreases with decreasing Pt coordination – caused by increased backbonding – with well-coordinated Pt (WC, 8- or 9-fold coordination) absorbing around 2098 – 2080 cm^{-1} and under-coordinated Pt (UC, <8-fold coordination) absorbing around 2075 – 2000 cm^{-1} [72–74]. Furthermore, high CO coverage can result in a shift to higher wavenumbers (blue shift) caused by dipole-dipole coupling of proximate CO molecules adsorbed on the Pt surface. A coverage-dependent shift was observed for F-Pt/Al_2O_3 during the temperature programmed desorption (TPD) under flowing He, with the peak center shifting from 2082 cm^{-1} to 2076 cm^{-1} (Figure S12). F-SE-Pt/Al_2O_3 and F-LE-Pt/Al_2O_3 exhibited no shift in peak center as CO desorbed (Figures S13-S14). These results indicated that the slight shift in peak center position between F-Pt/Al_2O_3 and F-SE-Pt/Al_2O_3 could be attributed to a difference in CO coverage on the surface (Figure 6d). The lack of a CO coverage-dependent shift in both fresh ALD samples suggested that some of the WC Pt sites were covered during the ALD process, leading to greater separation between binding sites and hence less coverage-dependent frequency shifts. The further red shift of the peak center for adsorbed CO on F-LE-Pt/Al_2O_3 could be attributed to a change in Pt binding sites, in line with the fact that the signal for CO bound to WC Pt sites was much attenuated in intensity (Figure 6c). The observed peak broadening indicated less uniform binding sites in the ALD samples compared to F-Pt/Al_2O_3. Overall, these observations revealed that compared to F-Pt/Al_2O_3, the CO binding sites in the ALD samples were more isolated, less uniform, and more undercoordinated.

The pronounced change in line shape after aging was consistent with the restructuring of the Pt and alumina overlayers observed by STEM and SSNMR. Interestingly, the samples that were stable against sintering (SE-Pt/Al_2O_3 and LE-Pt/Al_2O_3) showed a larger population of UC Pt^0 sites when compared to the control sample Pt/Al_2O_3 that showed particle sintering. Seminal work by Lu et al.[35] attributed the sintering stability of ALD alumina-coated Pd nanoparticles to the saturation of UC Pd atoms. However, our results demonstrated that after hydrothermal aging, a large population of UC sites became available for CO binding (and likely for reactivity) in the more stable catalysts (SE-Pt/Al_2O_3 and LE-Pt/Al_2O_3). It is likely that this difference was due to the specific pre- and post-treatments that were performed on these samples that modified the ALD alumina overlayers. The relative intensity of the peaks corresponding to UC Pt sites compared to WC Pt could also be used to assess particle size, as smaller particles have an increased contribution from UC species [75]. Given the relative intensity of the signals, the results in Figure 6 indicated that A-Pt/Al_2O_3 contained the largest particles and A-LE-Pt/Al_2O_3 contained the smallest particles, consistent with the particle size distributions from HAADF-STEM reported in Figure 4 and XRD results reported in Figure S3.

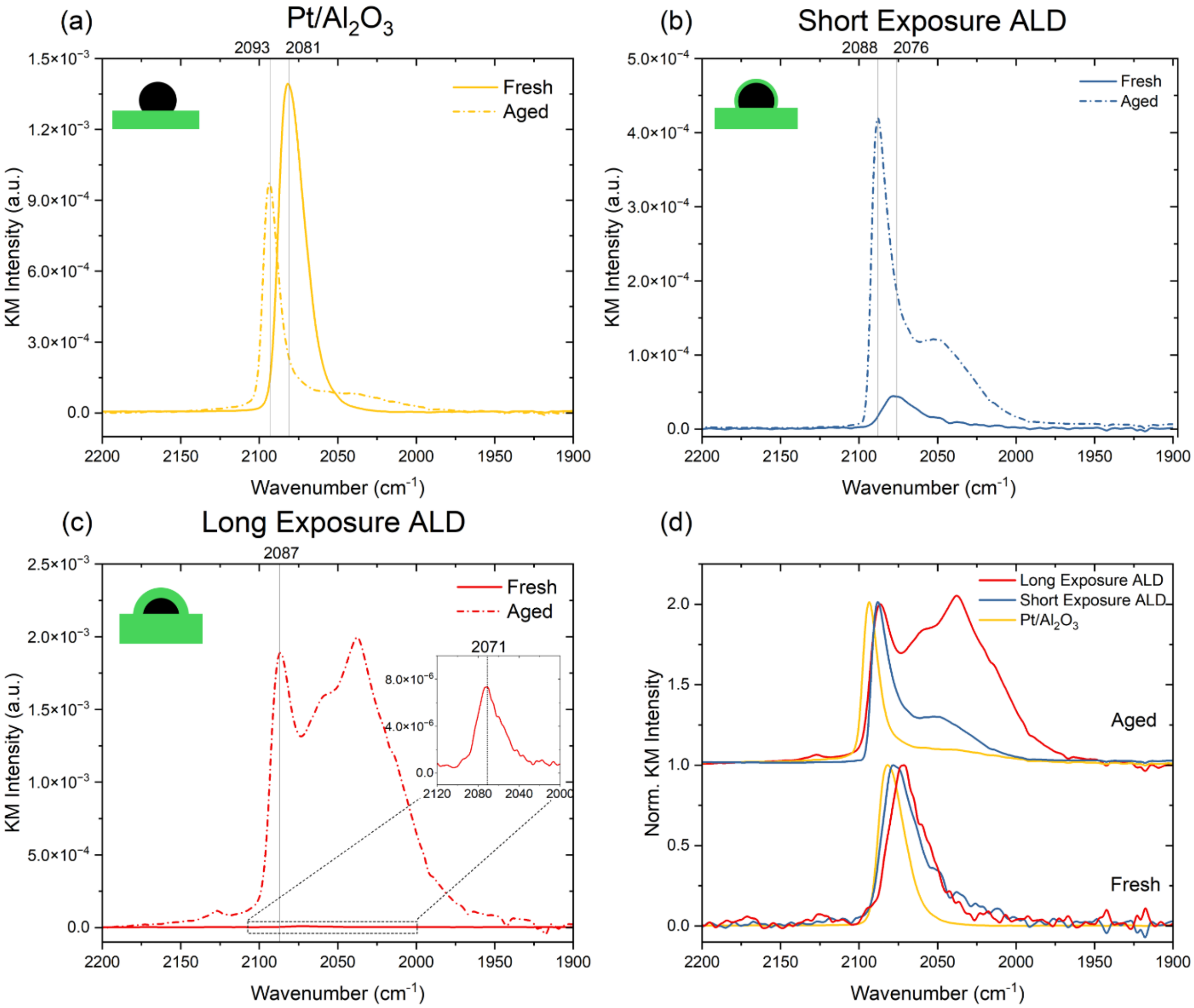

Figure 6. Raw DRIFT spectra of CO adsorbed at saturation coverage and room temperature for fresh and aged (a) Pt/Al_2O_3, (b) SE-Pt/Al_2O_3, and (c) LE-Pt/Al_2O_3 samples. The inset in panel c shows a zoomed in view of the F-LE-Pt/Al_2O_3 sample. (d) Comparison of normalized DRIFT spectra for all fresh and aged samples. Fresh spectra are normalized to maximum intensity. Aged spectra are normalized to the high wavenumber feature corresponding to well-coordinated Pt.

Understanding catalyst stability

In oxygen-rich high temperature environments, Ostwald ripening is well-recognized as a root cause for the extensive deterioration of Pt catalysts performance. This phenomenon is driven by the pronounced volatility of PtO_2, which can form on the surface of the Pt nanoparticle and at high temperatures will readily detach, going from smaller to larger nanoparticles. However, the minimal depletion of Pt from catalyst beds or monolithic structures poses a challenge for detecting small variation in Pt loading through conventional wet chemical analysis methods to demonstrate the origin of stability in engineered catalysts. An approach to observe and quantify the amount of Pt leaving a catalyst thin film via electron microscopy and EDS signal intensity measurements was used here following previous work.[76–78] Differing from the previous work, in which SEM-EDS was employed, this study opted for XRF due to its heightened sensitivity. This choice enabled greater accuracy and precision in quantifying the low loadings exhibited by these catalysts.

In Figure 7, the Pt loading is plotted as a function of time at 800 °C in flowing air and used as an indicator of the rate of Pt loss: the faster the loss, the more prone to sintering a catalyst was. The Pt/Al_2O_3 catalyst showed a complete loss of Pt signal within 90 minutes. The Pt signal decrease could initially be fit with an exponential decay for the first 60 minutes. Between 60 and 90 minutes, the more rapid Pt loading decrease aligned with the findings of Challa *et al.*[79], who proposed that nanoparticles, when approaching a certain size threshold (typically below ~2 nm), undergo a rapid increase in chemical potential due to the Gibbs-Thomson effect, consequently elevating vapor pressure and disappearing more rapidly than larger particles. The low Pt concentration in this final stage introduced substantial errors, making it harder to fit a model to this last portion of the dataset. In contrast, the SE- and LE-Pt/Al_2O_3 samples demonstrated a much slower Pt loading loss and still retained significant amounts of Pt over the same time span compared to the Pt/Al_2O_3 sample.

The data were fitted to an exponential decay model, as shown in equation (1):

$$W(t) = W_0 e^{-t/\tau} \qquad \text{(eq. 1)}$$

where W_0 denotes the initial weight fraction (%) of Pt in the catalyst at time $t = 0$, while W denotes the weight percentage at time t. Each sample's Pt content was normalized to unity. The time constant, denoted as τ, was then calculated by fitting the data, and it was found to be 45 minutes for Pt/Al_2O_3, 202 minutes for SE-Pt/Al_2O_3, and 552 minutes for LE-Pt/Al_2O_3. This time constant is inversely proportional to the Pt vapor pressure, as established by a model outlined in a previous study[78] based on well-established principles of surface evaporation.[80,81] Leveraging this model, we were able to assess the impact of ALD on the vapor pressure of PtO_2. When examining the time constants corresponding to each sample, it was clear that the introduction of alumina overlayers had a significant influence over the Pt's vapor phase transport. The Pt/Al_2O_3 sample experienced a rapid Pt loss. Following SE ALD, this time constant indicated a substantial 4.5-fold decrease in the Pt evaporation rate. With LE ALD, the time constant further indicated a notable 12-fold reduction in Pt evaporation rate compared to the untreated sample, and a 2.7-fold decrease compared to the SE ALD sample. This drastic change was consistent with the model's assumption that diffusion through alumina constituted the rate-limiting step. Consequently, the addition of alumina impeded Pt atoms from escaping the encapsulation layers and entering the vapor phase, thus inhibiting sintering. These measurements thus suggest that the inhibition of Ostwald ripening phenomena via reduced volatilization of the Pt was responsible for the increased stability in the ALD-modified samples.

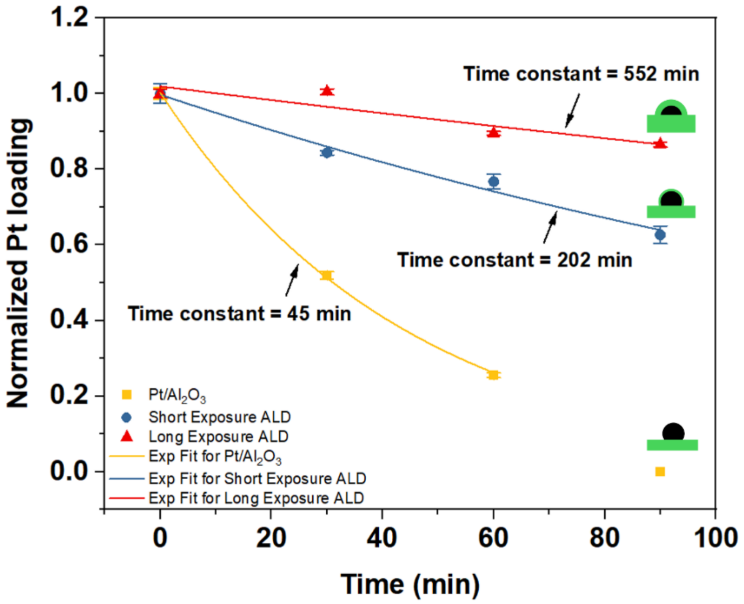

Figure 7. Normalized Pt loading measured on catalyst films as a function of time at 800 °C in flowing air.

Our findings indicate that samples characterized by the presence of less coordinated Pt^0 were not prone to sintering as previously anticipated. This could be explained by the introduction of an increased resistance to Pt transport due to the addition of the Al_2O_3 ALD overlayers. Pt species could potentially diffuse through both the vapor phase and the solid phase. As our measurements highlighted the inhibition of Pt vapor phase transport, we also want to investigate the possibility of Pt solid state diffusion. To elucidate this phenomenon, we investigated the energetics of diffusion and anchoring of Pt atoms through the ALD layers. We assessed metal binding energies using our recently developed coordination-based α-scheme model on various sites[82]. The predicted metal binding energies were found to be favorable for the binding of Pt to the ALD overlayer in defective Al vacancy sites. The calculated binding energies of Pt within Al defect sites within the most preferable intermediate i.e., $Al_2(OH)_6$ and the final compound Al_2O_3, were –5.29 and –7.89 eV, respectively, whereas Pt binding energy in Pt bulk was -6.01 eV (Figure 8(a-c)). Interestingly, it is found that Pt will bind very strongly to Al vacancies, with energetics that are either comparable (0.72 ΔeV for Al_2O_3 vs Pt) or much more favorable (-1.88 ΔeV for $Al_2(OH)_6$ vs Pt) compared to Pt bulk. Taken all together, the results showed that Pt atoms can favorably bind to the encapsulating overlayer, especially within defective sites, indicating that Pt is likely to remain within the encapsulating oxide rather than escaping in the vapor phase. Overall, this observation suggests a feasible pathway for Pt moieties to diffuse and find a new anchoring site within the ALD layers, preventing its normal ripening behavior, and thus inhibiting sintering. This diffusion process might also have contributions to the observed formation of small nanoclusters following the aging of the long exposure ALD sample (Figure 4f, Figures S6-7).

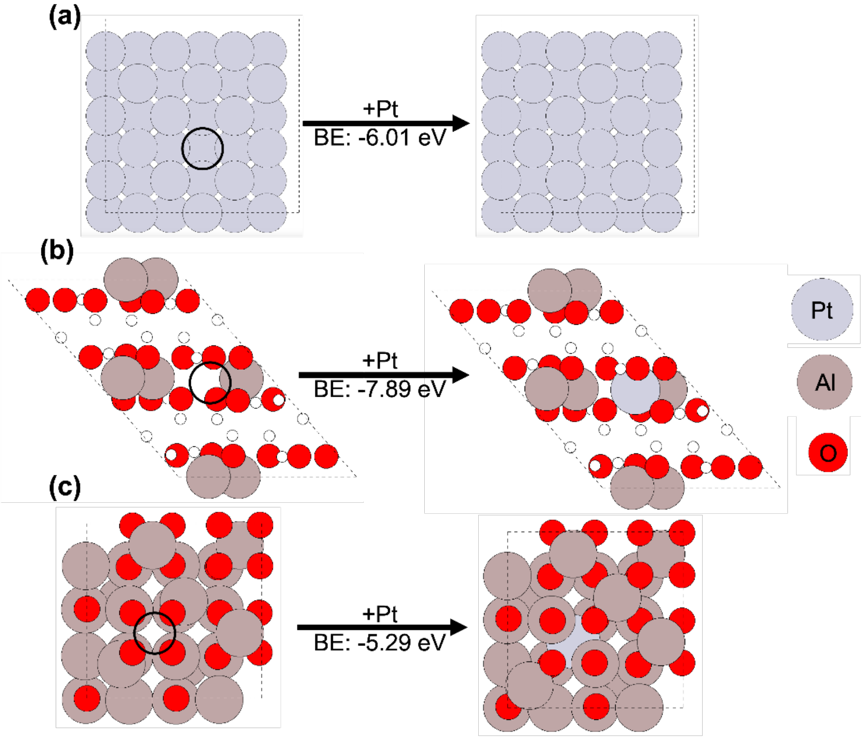

Figure 8. Calculated binding energies of Pt in (a) Pt bulk, (b) Al vacancy in $Al_2(OH)_6$, (c) Al vacancy in Al_2O_3. Atomic arrangements before (left) and after (right) Pt binding. Black circles identify vacancies.

To explain the Pt diffusion hypothesis, we calculated diffusion barriers using climbing-image nudged elastic band (CI-NEB) method[83]. In this context, we considered six images within reactants and products. We considered $Al_2(OH)_2$ vacancies within bulk $Al_2(OH)_6$ and the calculated diffusion barriers for Pt migration within the $Al_2(OH)_2$ defect were 0.86 and 1.16 eV, which could be easily overcome during the aging process (Figure Sx). It is noteworthy to mention that the Pt migration likely depends on defects in various ALD-based intermediates, temperature, and other reaction conditions, making the study more complex. However, the thermodynamic calculations and preliminary diffusion barriers of Pt within $Al_2(OH)_2$ vacancies in bulk $Al_2(OH)_6$ support our hypothesis that Pt can diffuse through ALD layers and form small nanoclusters during the aging process.

CONCLUSIONS

We showed that the addition of small amounts of alumina ALD (~3% of the initial catalyst mass) could inhibit Pt sintering in Pt/Al_2O_3 catalysts in relevant emission control reaction conditions. The greater stability of encapsulated Pt catalysts was found to improve the utilization efficiency of Pt by a factor of 2.5, more than halving the theoretical Pt mass needed to achieve the same performance for conventional supported catalysts. We demonstrated that the saturation of under-coordinated Pt^0 sites (edges, steps) by the alumina ALD layers could not explain the observed behavior. These sites were in fact abundant in stable encapsulated catalysts after aging, according to CO DRIFTS results. On the other hand, the inhibition of Pt vapor phase transport correlated well with catalyst stability, pointing at the suppression of Ostwald ripening phenomena as the root cause of sintering prevention. This result highlights the role of the oxide overlayer as a physical barrier to mass transport and a potential anchoring site for Pt atoms, as confirmed by DFT calculations. Overall, this work elucidates the role and potential of thin encapsulating oxide overlayers in decreasing noble metal particle sintering and increasing noble metal utilization efficiency in emission control catalysts.

SUPPORTING INFORMATION

CO_2 production rate against time on stream. Model Pt nanoparticle and ALD process. XPS survey scans. Additional TEM micrographs of A-LE-Pt/Al_2O_3. N_2 adsorption and desorption isotherms with BJH adsorption pore size distribution of all samples. XRD patterns of aged samples. High resolution XPS of Al 2p region for aged catalysts. CO TPD DRIFTS spectra. XRF Al/Pt mass ratio. Possible ALD intermediates.

ACKNOWLEDGEMENTS

GL acknowledges Simon R. Bare for his support throughout this project. This work was supported by the U.S. Department of Energy, Office of Science, Office of Basic Energy Sciences, under contract no. DE-SC0022197. Part of this work was performed at the Stanford Nano Shared Facilities (SNSF), supported by the National Science Foundation under award ECCS-2026822. LC acknowledges support from the National Science Foundation Award #2001189. P.N.P. acknowledges funding by Deutsche Forschungsgemeinschaft (DFG, German Research Foundation) - SFB 1441 - Project ID 426888090. Electron microscopy is performed at the Center for Nanophase Materials Sciences (CNMS), which is a US Department of Energy, Office of Science User Facility at Oak Ridge National Laboratory.

REFERENCES

(1) Armor, J. N. A History of Industrial Catalysis. *Catal Today* **2011**, *163* (1), 3–9.

(2) Seymour, R. J.; O'Farrelly, J. Platinum-Group Metals. *Kirk-Othmer Encyclopedia of Chemical Technology* **2012**, 1–37.

(3) Hughes, A. E.; Haque, N.; Northey, S. A.; Giddey, S. Platinum Group Metals: A Review of Resources, Production and Usage with a Focus on Catalysts. *Resources 2021, Vol. 10, Page 93* **2021**, *10* (9), 93.

(4) Mudd, G. M.; Jowitt, S. M.; Werner, T. T. Global Platinum Group Element Resources, Reserves and Mining – A Critical Assessment. *Science of The Total Environment* **2018**, *622–623*, 614–625.

(5) Cowley, A.; Jiang, J.; Tang, B.; Wang, A.; Bloxham, L.; Brown, S.; Cole, L.; Fujita, M.; Girardot, N.; Raithatha, R.; Ryan, M. The PGM Market Report Is Written by Alison Cowley. Special Feature Written.

(6) Burlakovs, J.; Vincevica-Gaile, Z.; Krievans, M.; Jani, Y.; Horttanainen, M.; Pehme, K. M.; Dace, E.; Setyobudi, R. H.; Pilecka, J.; Denafas, G.; Grinfelde, I.; Bhatnagar, A.; Rud, V.; Rudovica, V.; Mersky, R. L.; Anne, O.; Kriipsalu, M.; Ozola-Davidane, R.; Tamm, T.; Klavins, M. Platinum Group Elements in Geosphere and Anthroposphere: Interplay among the Global Reserves, Urban Ores, Markets and Circular Economy. *Minerals 2020, Vol. 10, Page 558* **2020**, *10* (6), 558.

(7) Hughes, A. E.; Haque, N.; Northey, S. A.; Giddey, S. Platinum Group Metals: A Review of Resources, Production and Usage with a Focus on Catalysts. *Resources 2021, Vol. 10, Page 93* **2021**, *10* (9), 93.

(8) *Ecotrade Group | Future of auto catalyst configurations, impact on PGMs, and implications for collectors*. https://www.ecotradegroup.com/en/blog/future-complexities-of-auto-catalyst-

configurations-their-impact-on-platinum-group-metals-and-the-implications-for-collectors (accessed 2023-06-28).

(9) Kalantar Neyestanaki, A.; Klingstedt, F.; Salmi, T.; Murzin, D. Y. Deactivation of Postcombustion Catalysts, a Review. *Fuel* **2004**, *83* (4–5), 395–408.

(10) Wallington, T. J.; Anderson, J. E.; Dolan, R. H.; Winkler, S. L. Vehicle Emissions and Urban Air Quality: 60 Years of Progress. *Atmosphere 2022, Vol. 13, Page 650* **2022**, *13* (5), 650.

(11) Serpe, A.; Bigoli, F.; Cabras, M. C.; Fornasiero, P.; Graziani, M.; Mercuri, M. L.; Montini, T.; Pilia, L.; Trogu, E. F.; Deplano, P. Pd-Dissolution through a Mild and Effective One-Step Reaction and Its Application for Pd-Recovery from Spent Catalytic Converters. *Chemical Communications* **2005**, No. 8, 1040–1042.

(12) Chidunchi, I.; Kulikov, M.; Safarov, R.; Kopishev, E. Extraction of Platinum Group Metals from Catalytic Converters. **2024**.

(13) Jimenez De Aberasturi, D.; Pinedo, R.; Ruiz De Larramendi, I.; Ruiz De Larramendi, J. I.; Rojo, T. Recovery by Hydrometallurgical Extraction of the Platinum-Group Metals from Car Catalytic Converters. *Miner Eng* **2011**, *24* (6), 505–513.

(14) Baker, R. T. K.; Thomas, C.; Thomas, R. B. Continuous Observation of the Particle Size Behavior of Platinum on Alumina. *J Catal* **1975**, *38* (1–3), 510–513.

(15) Simonsen, S. B.; Chorkendorff, I.; Dahl, S.; Skoglundh, M.; Sehested, J.; Helveg, S. Ostwald Ripening in a Pt/SiO2 Model Catalyst Studied by in Situ TEM. *J Catal* **2011**, *281* (1), 147–155.

(16) Auvray, X.; Pingel, T.; Olsson, E.; Olsson, L. The Effect Gas Composition during Thermal Aging on the Dispersion and NO Oxidation Activity over Pt/Al2O3 Catalysts. *Appl Catal B* **2013**, *129*, 517–527.

(17) Dai, Y.; Lu, P.; Cao, Z.; Campbell, C. T.; Xia, Y. The Physical Chemistry and Materials Science behind Sinter-Resistant Catalysts. *Chem Soc Rev* **2018**, *47* (12), 4314–4331.

(18) Oh, J.; Beck, A.; Goodman, E. D.; Roling, L. T.; Boucly, A.; Artiglia, L.; Abild-Pedersen, F.; van Bokhoven, J. A.; Cargnello, M. Colloidally Engineered Pd and Pt Catalysts Distinguish Surface- and Vapor-Mediated Deactivation Mechanisms. *ACS Catal* **2023**, *13* (3), 1812–1822.

(19) Goodman, E. D.; Schwalbe, J. A.; Cargnello, M. Mechanistic Understanding and the Rational Design of Sinter- Resistant Heterogeneous Catalysts. *ACS Catal* **2017**, *7* (10), 7156–7173.

(20) Farago, M. E.; Hutchinson, E. J.; Simpson, P. R.; Thornton, I. Recent Increases in Platinum Metals in the Environment from Vehicle Catalytic Converters. *https://doi-org.stanford.idm.oclc.org/10.1179/037174505X45531* **2005**, *114* (3).

(21) Helmers, E. Platinum Emission Rate of Automobiles with Catalytic Converters. *Environmental Science and Pollution Research* **1997**, *4* (2), 99–103.

(22) Hansen, T. W.; Delariva, A. T.; Challa, S. R.; Datye, A. K. Sintering of Catalytic Nanoparticles: Particle Migration or Ostwald Ripening? *Acc Chem Res* **2013**, *46* (8), 1720–1730.

(23) Wang, Y.; Wang, J.; Zheng, P.; Sun, C.; Luo, J.; Xie, X. Boosting Selectivity and Stability on Pt/BN Catalysts for Propane Dehydrogenation via Calcination & Reduction-Mediated Strong Metal-Support Interaction. *Journal of Energy Chemistry* **2022**, *67*, 451–457.

(24) Chen, H.; Yang, S. Z.; Yang, Z.; Lin, W.; Xu, H.; Wan, Q.; Suo, X.; Wang, T.; Jiang, D. E.; Fu, J.; Dai, S. Sinter-Resistant Nanoparticle Catalysts Achieved by 2D Boron Nitride-Based Strong Metal-Support Interactions: A New Twist on an Old Story. *ACS Cent Sci* **2020**, *6* (9), 1617–1627.

(25) Cao, Y.; Ran, R.; Wu, X.; Si, Z.; Kang, F.; Weng, D. Progress on Metal-Support Interactions in Pd-Based Catalysts for Automobile Emission Control. *Journal of Environmental Sciences* **2023**, *125*, 401–426.

(26) Li, W. J.; Wey, M. Y. Core-Shell Design and Well-Dispersed Pd Particles for Three-Way Catalysis: Effect of Halloysite Nanotubes Functionalized with Schiff Base. *Science of The Total Environment* **2019**, *675*, 397–407.

(27) Spezzati, G.; Su, Y.; Hofmann, J. P.; Benavidez, A. D.; DeLaRiva, A. T.; McCabe, J.; Datye, A. K.; Hensen, E. J. M. Atomically Dispersed Pd-O Species on CeO2(111) as Highly Active Sites for Low-Temperature CO Oxidation. *ACS Catal* **2017**, *7* (10), 6887–6891.

(28) Nagai, Y.; Hirabayashi, T.; Dohmae, K.; Takagi, N.; Minami, T.; Shinjoh, H.; Matsumoto, S. Sintering Inhibition Mechanism of Platinum Supported on Ceria-Based Oxide and Pt-Oxide–Support Interaction. *J Catal* **2006**, *242* (1), 103–109.

(29) Farmer, J. A.; Campbell, C. T. Ceria Maintains Smaller Metal Catalyst Particles by Strong Metal-Support Bonding. *Science (1979)* **2010**, *329* (5994), 933–936.

(30) Jones, J.; Xiong, H.; DeLaRiva, A. T.; Peterson, E. J.; Pham, H.; Challa, S. R.; Qi, G.; Oh, S.; Wiebenga, M. H.; Hernández, X. I. P.; Wang, Y.; Datye, A. K. Thermally Stable Single-Atom Platinum-on-Ceria Catalysts via Atom Trapping. *Science (1979)* **2016**, *353* (6295), 150–154.

(31) Yang, X.; Li, Q.; Lu, E.; Wang, Z.; Gong, X.; Yu, Z.; Guo, Y.; Wang, L.; Guo, Y.; Zhan, W.; Zhang, J.; Dai, S. Taming the Stability of Pd Active Phases through a Compartmentalizing Strategy toward Nanostructured Catalyst Supports. *Nature Communications 2019 10:1* **2019**, *10* (1), 1–9.

(32) Wang, G.; Xu, S.; Wang, L.; Liu, Z.; Dong, X.; Wang, L.; Zheng, A.; Meng, X.; Xiao, F. S. Fish-in-Hole: Rationally Positioning Palladium into Traps of Zeolite Crystals for Sinter-Resistant Catalysts. *Chemical Communications* **2018**, *54* (26), 3274–3277.

(33) Liu, J.; Ji, Q.; Imai, T.; Ariga, K.; Abe, H. Sintering-Resistant Nanoparticles in Wide-Mouthed Compartments for Sustained Catalytic Performance OPEN. *Nature Publishing Group* **2017**.

(34) Aitbekova, A.; Zhou, C.; Stone, M. L.; Lezama-Pacheco, J. S.; Yang, A. C.; Hoffman, A. S.; Goodman, E. D.; Huber, P.; Stebbins, J. F.; Bustillo, K. C.; Ercius, P.; Ciston, J.; Bare, S. R.; Plessow, P. N.; Cargnello, M. Templated Encapsulation of Platinum-Based Catalysts Promotes High-Temperature Stability to 1,100 °C. *Nature Materials 2022 21:11* **2022**, *21* (11), 1290–1297. https://doi.org/10.1038/s41563-022-01376-1.

(35) Lu, J.; Fu, B.; Kung, M. C.; Xiao, G.; Elam, J. W.; Kung, H. H.; Stair, P. C. Coking- and Sintering-Resistant Palladium Catalysts Achieved through Atomic Layer Deposition. *Science (1979)* **2012**, *335* (6073), 1205–1208.

(36) Kónya, Z.; Puntes, V. F.; Kiricsi, I.; Zhu, J.; Alivisatos, P.; Somorjai, G. A. Novel Two-Step Synthesis of Controlled Size and Shape Platinum Nanoparticles Encapsulated in Mesoporous Silica. *Catal Letters* **2002**, *81* (3–4), 137–140.

(37) Lee, I.; Zhang, Q.; Ge, J.; Yin, Y.; Zaera, F. Encapsulation of Supported Pt Nanoparticles with Mesoporous Silica for Increased Catalyst Stability. *Nano Res* **2011**, *4* (1), 115–123.

(38) Joo, S. H.; Park, J. Y.; Tsung, C. K.; Yamada, Y.; Yang, P.; Somorjai, G. A. Thermally Stable Pt/Mesoporous Silica Core–Shell Nanocatalysts for High-Temperature Reactions. *Nature Materials 2009 8:2* **2008**, *8* (2), 126–131.

(39) Liang, X.; Li, J.; Yu, M.; McMurray, C. N.; Falconer, J. L.; Weimer, A. W. Stabilization of Supported Metal Nanoparticles Using an Ultrathin Porous Shell. *ACS Catal* **2011**, *1* (10), 1162–1165.

(40) Onn, T. M.; Zhang, S.; Arroyo-Ramirez, L.; Chung, Y. C.; Graham, G. W.; Pan, X.; Gorte, R. J. Improved Thermal Stability and Methane-Oxidation Activity of Pd/Al2O3 Catalysts by Atomic Layer Deposition of ZrO2. *ACS Catal* **2015**, *5* (10), 5696–5701.

(41) Cargnello, M.; Doan-Nguyen, V. V. T.; Gordon, T. R.; Diaz, R. E.; Stach, E. A.; Gorte, R. J.; Fornasiero, P.; Murray, C. B. Control of Metal Nanocrystal Size Reveals Metal-Support Interface Role for Ceria Catalysts.

(42) Perrichon, V.; Laachir, A.; Abouarnadasse, S.; Touret, O.; Blanchard, G. Thermal Stability of a High Surface Area Ceria under Reducing Atmosphere. *Appl Catal A Gen* **1995**, *129* (1), 69–82.

(43) Gorte, R. J. Ceria in Catalysis: From Automotive Applications to the Water–Gas Shift Reaction. *AIChE Journal* **2010**, *56* (5), 1126–1135.

(44) Gatica, J. M.; Baker, R. T.; Fornasiero, P.; Bernal, S.; Kašpar, J. Characterization of the Metal Phase in NM/Ce0.68Zr0.32O2 (NM: Pt and Pd) Catalysts by Hydrogen Chemisorption and HRTEM Microscopy: A Comparative Study. *Journal of Physical Chemistry B* **2001**, *105* (6), 1191–1199.

(45) Fornasiero, P.; Kašpar, J.; Sergo, V.; Graziani, M. Redox Behavior of High-Surface-Area Rh-, Pt-, and Pd-Loaded Ce0.5Zr0.5O2Mixed Oxide. *J Catal* **1999**, *182* (1), 56–69.

(46) Schwab, M. G.; Fassbender, B.; Spiess, H. W.; Thomas, A.; Feng, X.; Müllen, K. Catalyst-Free Preparation of Melamine-Based Microporous Polymer Networks through Schiff Base Chemistry. *J Am Chem Soc* **2009**, *131* (21), 7216–7217.

(47) Cargnello, M.; Chen, C.; Diroll, B. T.; Doan-Nguyen, V. V. T.; Gorte, R. J.; Murray, C. B. Efficient Removal of Organic Ligands from Supported Nanocrystals by Fast Thermal Annealing Enables Catalytic Studies on Well-Defined Active Phases. *J Am Chem Soc* **2015**, *137* (21), 6906–6911.

(48) Libera, J. A.; Elam, J. W.; Pellin, M. J. Conformal ZnO Coatings on High Surface Area Silica Gel Using Atomic Layer Deposition. *Thin Solid Films* **2008**, *516* (18), 6158–6166.

(49) Hjorth Larsen, A.; JØrgen Mortensen, J.; Blomqvist, J.; Castelli, I. E.; Christensen, R.; Dułak, M.; Friis, J.; Groves, M. N.; Hammer, B.; Hargus, C.; Hermes, E. D.; Jennings, P. C.; Bjerre Jensen, P.; Kermode, J.; Kitchin, J. R.; Leonhard Kolsbjerg, E.; Kubal, J.; Kaasbjerg, K.; Lysgaard, S.; Bergmann Maronsson, J.; Maxson, T.; Olsen, T.; Pastewka, L.; Peterson, A.; Rostgaard, C.;

SchiØtz, J.; Schütt, O.; Strange, M.; Thygesen, K. S.; Vegge, T.; Vilhelmsen, L.; Walter, M.; Zeng, Z.; Jacobsen, K. W. The Atomic Simulation Environment—a Python Library for Working with Atoms. *Journal of Physics: Condensed Matter* **2017**, *29* (27), 273002.

(50) Kresse, G.; Furthmüller, J. Efficient Iterative Schemes for *Ab Initio* Total-Energy Calculations Using a Plane-Wave Basis Set. *Phys Rev B* **1996**, *54* (16), 11169.

(51) Kresse, G.; Furthmüller, J. Efficiency of Ab-Initio Total Energy Calculations for Metals and Semiconductors Using a Plane-Wave Basis Set. *Comput Mater Sci* **1996**, *6* (1), 15–50.

(52) Kresse, G.; Hafner, J. *Ab Initio* Molecular Dynamics for Liquid Metals. *Phys Rev B* **1993**, *47* (1), 558.

(53) Lee, K.; Murray, É. D.; Kong, L.; Lundqvist, B. I.; Langreth, D. C. Higher-Accuracy van Der Waals Density Functional. *Phys Rev B Condens Matter Mater Phys* **2010**, *82* (8), 081101.

(54) Wellendorff, J.; Lundgaard, K. T.; Møgelhøj, A.; Petzold, V.; Landis, D. D.; Nørskov, J. K.; Bligaard, T.; Jacobsen, K. W. Density Functionals for Surface Science: Exchange-Correlation Model Development with Bayesian Error Estimation. *Phys Rev B Condens Matter Mater Phys* **2012**, *85* (23), 235149.

(55) Tahsini, N.; Yang, A. C.; Streibel, V.; Werghi, B.; Goodman, E. D.; Aitbekova, A.; Bare, S. R.; Li, Y.; Abild-Pedersen, F.; Cargnello, M. Colloidal Platinum-Copper Nanocrystal Alloy Catalysts Surpass Platinum in Low-Temperature Propene Combustion. *J Am Chem Soc* **2022**, *144* (4), 1612–1621.

(56) Monkhorst, H. J.; Pack, J. D. Special Points for Brillouin-Zone Integrations. *Phys Rev B* **1976**, *13* (12), 5188.

(57) Bengtsson, L. Dipole Correction for Surface Supercell Calculations. *Phys Rev B* **1999**, *59* (19), 12301.

(58) Mandal, S. C.; Abild-Pedersen, F. Classification of Adsorbed Hydrocarbons Based on Bonding Configurations of the Adsorbates and Surface Site Stabilities. *ACS Catal* **2023**, *13*, 13663–13671.

(59) Roling, L. T.; Li, L.; Abild-Pedersen, F. Configurational Energies of Nanoparticles Based on Metal-Metal Coordination. *Journal of Physical Chemistry C* **2017**, *121* (41), 23002–23010.

(60) Streibel, V.; Aljama, H. A.; Yang, A. C.; Choksi, T. S.; Sánchez-Carrera, R. S.; Schäfer, A.; Li, Y.; Cargnello, M.; Abild-Pedersen, F. Microkinetic Modeling of Propene Combustion on a Stepped, Metallic Palladium Surface and the Importance of Oxygen Coverage. *ACS Catal* **2022**, *12* (3), 1742–1757.

(61) Winther, K. T.; Hoffmann, M. J.; Boes, J. R.; Mamun, O.; Bajdich, M.; Bligaard, T. Catalysis-Hub.Org, an Open Electronic Structure Database for Surface Reactions. *Scientific Data 2019 6:1* **2019**, *6* (1), 1–10.

(62) Mei, Z.; Li, Y.; Fan, M.; Zhao, L.; Zhao, J. Effect of the Interactions between Pt Species and Ceria on Pt/Ceria Catalysts for Water Gas Shift: The XPS Studies. *Chemical Engineering Journal* **2015**, *259*, 293–302.

(63) Ramallo-López, J. M.; Santori, G. F.; Giovanetti, L.; Casella, M. L.; Ferretti, O. A.; Requejo, F. G. XPS and XAFS Pt L2,3-Edge Studies of Dispersed Metallic Pt and PtSn Clusters on SiO2

Obtained by Organometallic Synthesis: Structural and Electronic Characteristics. *Journal of Physical Chemistry B* **2003**, *107* (41), 11441–11451.

(64) Kim, C. R.; Lee, J. Y.; Heo, J. H.; Shin, C. M.; Lee, T. M.; Park, J. H.; Ryu, H.; Chang, J. H.; Son, C. S. Effects of Annealing Temperature and Al2O3 Buffer Layer on ZnO Thin Films Grown by Atomic Layer Deposition. *Current Applied Physics* **2010**, *10* (2), S298–S301.

(65) Lee, S. K.; Park, S. Y.; Yi, Y. S.; Moon, J. Structure and Disorder in Amorphous Alumina Thin Films: Insights from High-Resolution Solid-State NMR. *Journal of Physical Chemistry C* **2010**, *114* (32), 13890–13894.

(66) Lee, S. K.; Park, S. Y.; Yi, Y. S.; Moon, J. Structure and Disorder in Amorphous Alumina Thin Films: Insights from High-Resolution Solid-State NMR. *Journal of Physical Chemistry C* **2010**, *114* (32), 13890–13894.

(67) Primet, M.; Basset, J. M.; Mathieu, M. V.; Prettre, M. Infrared Study of CO Adsorbed on PtAl2O3. A Method for Determining Metal-Adsorbate Interactions. *J Catal* **1973**, *29* (2), 213–223.

(68) Robatjazi, H.; Battsengel, T.; Finzel, J.; Tieu, P.; Xu, M.; Hoffman, A. S.; Qi, J.; Bare, S. R.; Pan, X.; Chmelka, B. F.; Halas, N. J.; Christopher, P. Dynamic Behavior of Platinum Atoms and Clusters in the Native Oxide Layer of Aluminum Nanocrystals. *ACS Nano* **2024**, *18* (8), 6638–6649.

(69) Lentz, C.; Jand, S. P.; Melke, J.; Roth, C.; Kaghazchi, P. DRIFTS Study of CO Adsorption on Pt Nanoparticles Supported by DFT Calculations. *J Mol Catal A Chem* **2017**, *426*, 1–9.

(70) Siemer, M.; Tomaschun, G.; Klüner, T.; Christopher, P.; Christopher, P.; Al-Shamery, K. Insights into Spectator-Directed Catalysis: CO Adsorption on Amine-Capped Platinum Nanoparticles on Oxide Supports. *ACS Appl Mater Interfaces* **2020**, *12* (24), 27765–27776.

(71) Hoffman, A. S.; Fang, C. Y.; Gates, B. C. Homogeneity of Surface Sites in Supported Single-Site Metal Catalysts: Assessment with Band Widths of Metal Carbonyl Infrared Spectra. *Journal of Physical Chemistry Letters* **2016**, *7* (19), 3854–3860.

(72) Siemer, M.; Tomaschun, G.; Klüner, T.; Christopher, P.; Christopher, P.; Al-Shamery, K. Insights into Spectator-Directed Catalysis: CO Adsorption on Amine-Capped Platinum Nanoparticles on Oxide Supports. *ACS Appl Mater Interfaces* **2020**, *12* (24), 27765–27776.

(73) Avanesian, T.; Dai, S.; Kale, M. J.; Graham, G. W.; Pan, X.; Christopher, P. Quantitative and Atomic-Scale View of CO-Induced Pt Nanoparticle Surface Reconstruction at Saturation Coverage via DFT Calculations Coupled with in Situ TEM and IR. *J Am Chem Soc* **2017**, *139* (12), 4551–4558.

(74) Kale, M. J.; Christopher, P. Utilizing Quantitative in Situ FTIR Spectroscopy to Identify Well-Coordinated Pt Atoms as the Active Site for CO Oxidation on Al2O3-Supported Pt Catalysts. *ACS Catal* **2016**, *6* (8), 5599–5609.

(75) Kale, M. J.; Christopher, P. Utilizing Quantitative in Situ FTIR Spectroscopy to Identify Well-Coordinated Pt Atoms as the Active Site for CO Oxidation on Al2O3-Supported Pt Catalysts. *ACS Catal* **2016**, *6* (8), 5599–5609.

(76) Leistner, K.; Gonzalez Braga, C.; Kumar, A.; Kamasamudram, K.; Olsson, L. Volatilisation and Subsequent Deposition of Platinum Oxides from Diesel Oxidation Catalysts. *Appl Catal B* **2019**, *241*, 338–350.

(77) Ghosh, A.; Pham, H.; Higgins, J.; Van Swol, F.; DeLaRiva, A.; Melton, M.; Kunwar, D.; Qi, G.; Oh, S. H.; Wiebenga, M.; Li, W.; Datye, A. K. Restricting the Growth of Pt Nanoparticles through Confinement in Ordered Nanoporous Structures. *Appl Catal A Gen* **2020**, *607*, 117858.

(78) Porter, S.; Ghosh, A.; Liu, C. H.; Kunwar, D.; Thompson, C.; Alcala, R.; Dean, D. P.; Miller, J. T.; DeLaRiva, A.; Pham, H.; Peterson, E.; Brearley, A.; Watt, J.; Kyriakidou, E. A.; Datye, A. K. Biphasic Janus Particles Explain Self-Healing in Pt-Pd Diesel Oxidation Catalysts. *ACS Catal* **2023**, *13* (8), 5456–5471.

(79) Challa, S. R.; Delariva, A. T.; Hansen, T. W.; Helveg, S.; Sehested, J.; Hansen, P. L.; Garzon, F.; Datye, A. K. Relating Rates of Catalyst Sintering to the Disappearance of Individual Nanoparticles during Ostwald Ripening. *J Am Chem Soc* **2011**, *133* (51), 20672–20675.

(80) Langmuir, I. The Vapor Pressure of Metallic Tungsten. *Physical Review* **1913**, *2* (5), 329.

(81) Fonda, G. R. Evaporation Characteristics of Tungsten. *Physical Review* **1923**, *21* (3), 343.

(82) Roling, L. T.; Li, L.; Abild-Pedersen, F. Configurational Energies of Nanoparticles Based on Metal-Metal Coordination. *Journal of Physical Chemistry C* **2017**, *121* (41), 23002–23010.

(83) Henkelman, G.; Blas, ; Uberuaga, P.; Jónsson, H.; Uberuaga, B. P.; Jó, H. A Climbing Image Nudged Elastic Band Method for Finding Saddle Points and Minimum Energy Paths. *J Chem Phys* **2000**, *113* (22), 9901–9904.

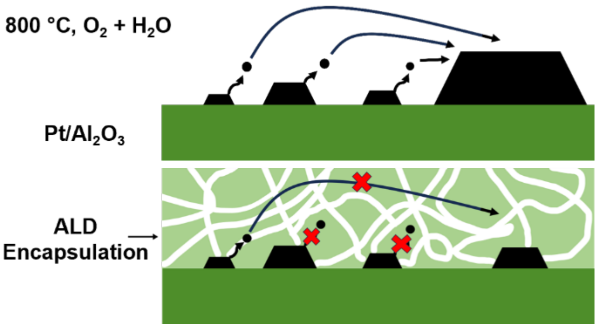

For table of contents only